ASSERT Program, "Thermomechanical Behavior of Functionally Graded Materials (FGM)"

Final Report to AFOSR F49620-97-1-0420

November 15, 2001

Steven Hudnut

Minoru Taya

Center for Intelligent Materials and Systems, Department of Mechanical Engineering, University of Washington, Seattle, Washington 98195

20020130 241

REPORT DOCUMENTATION PAGE

AFRL-SR-BL-TR-02-

0012

The public reporting burden for this collection of information is estimated to average 1 hour per response, including gathering and maintaining the data needed, and completing and reviewing the collection of information. Send commen of information, including suggestions for reducing the burden, to Department of Defense, Washington Headqua (0704-0188), 1215 Jefferson Davis Highway, Suite 1204, Arlington, VA 22202-4302. Respondents should be awar subject to any penalty for failing to comply with a collection of information if it does not display a currently valid OMB c
PLEASE DO NOT RETURN YOUR FORM TO THE ABOVE ADDRESS.

1. REPORT DATE (DD-MM-YYYY)	2. REPORT TYPE	3. DATES COVERED (From - To)
15-11-2001	Final Report	01 June 1997 - 31 December 2000

4. TITLE AND SUBTITLE
ASSERT Program,
"Thermomechanical Behavior of Functionally Graded Materials (FGM)"

5a. CONTRACT NUMBER
F49620-97-1-0420

5b. GRANT NUMBER

5c. PROGRAM ELEMENT NUMBER

6. AUTHOR(S)
Hudnut, Steven and Taya, Minoru

5d. PROJECT NUMBER

5e. TASK NUMBER

5f. WORK UNIT NUMBER

7. PERFORMING ORGANIZATION NAME(S) AND ADDRESS(ES)
Center for Intelligent Materials and Systems (CIMS)
Department of Mechanical Engineering
University of Washington, Box 352600
Seattle, WA 98195-2600

8. PERFORMING ORGANIZATION REPORT NUMBER

9. SPONSORING/MONITORING AGENCY NAME(S) AND ADDRESS(ES)
Air Force Office of Scientific Reserach
Directorate of Aerospace and Material Sciences
AFOSR/NA
801 Arlington, VA 22203-1977

10. SPONSOR/MONITOR'S ACRONYM(S)
AFOSR

11. SPONSOR/MONITOR'S REPORT NUMBER(S)

12. DISTRIBUTION/AVAILABILITY STATEMENT
unlimited

AIR FORCE OFFICE OF SCIENTIFIC RESEARCH (AFOSR)
NOTICE OF TRANSMITTAL DTIC. THIS TECHNICAL REPORT
HAS BEEN REVIEWED AND IS APPROVED FOR PUBLIC RELEASE
LAW AFR 190-12. DISTRIBUTION IS UNLIMITED.

13. SUPPLEMENTARY NOTES

14. ABSTRACT

This final report is to document a summary of Ph.D Student, Mr. Steven Hudnut who was supported by this ASSERT Grant, working on design of Piezo Actuators with Functionally Graded Microstructure (FGM). Mr. Hudnut has achieved both analytical modeling of several FGM piezo-laminate actuators with aim of maximizing the bending displacement while minimizing the internal stress, thus enhancing its fatigue life.

Mr. Hudnut designed a new laser displacement measurement apparatus by which the bending performance of bimorph and bimorph FGM piezo-actuators are characterized. He also contributed to the construction of lamination model for piezo laminated composites, as well as optimization of the FGM bimorph actuator mode of continuous piezo fibers.

15. SUBJECT TERMS

16. SECURITY CLASSIFICATION OF:			17. LIMITATION OF ABSTRACT	18. NUMBER OF PAGES	19a. NAME OF RESPONSIBLE PERSON
a. REPORT	b. ABSTRACT	c. THIS PAGE		24	Minoru Taya
					19b. TELEPHONE NUMBER (Include area code) (206) 685-2850

Abstract

This final report is to document a summary of Ph.D Student, Mr. Steven Hudnut who was supported by this ASSERT Grant, working on design of Piezo Actuators with Functionally Graded Microstructure (FGM). Mr. Hudnut has achieved both analytical modeling of several FGM piezo-laminate actuators with aim of maximizing the bending displacement while minimizing the internal stress, thus enhancing its fatigue life.

Mr. Hudnut designed a new laser displacement measurement apparatus by which the bending performance of bimorph and bimorph FGM piezo-actuators are characterized. He also contributed to the construction of lamination model for piezo laminated composites, as well as optimization of the FGM bimorph actuator mode of continuous piezo fibers.

Table of contents page

1. Modeling Of Piezoelectric FGM Plates 4

1.1 Classical Lamination Theory 5

1.2 2D Elasticity Model For Piezo Composite Laminates in Cylindrical Bending 7

2. Material Property Modeling For Fiber Based Piezoelectric FGM Bimorphs.....14

2.1 The Fiber Based Piezoelectric FGM Bimorph 14

2.2 Modeling Fiber Based Piezoelectric Composite Material Properties...15

2.3 Analysis Of The Piezoelectric Fiber Based FGM Bimorph 20

3. Design of Laser Displacement Measurement System.....22

4. Concluding Remarks And Future Work.....23

5. References 24

1. Modeling Of A Piezoelectric FGM Plate

Analytical study on piezoelectric laminate with functionally graded microstructure (FGM) was established to construct a hierarchical modeling (Almajid *et. al.* (2000)). The study consist of two models, one at microscopic level focusing on the microstructure of each FGM layer, the other on laminating FGM layers to predict the out-of-plane displacement of the FGM plate under applied electric field. The standard piezoelectric actuator plate is of bimorph type. These kinds of actuators develop high stresses in the interface between the materials as shown in Figure 11. An FGM model has been investigated to reduce the otherwise high stresses. FGM have shown a remarkable reduction of the residual stresses.

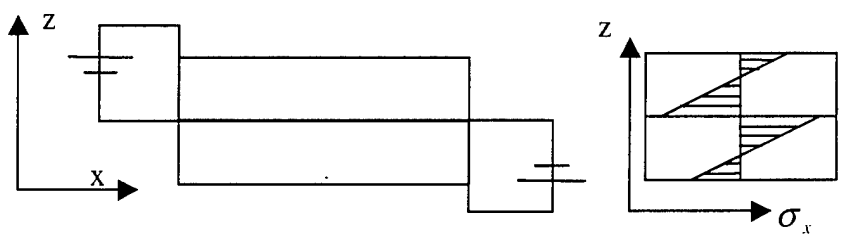

Figure 11 Typical stresses generated in a bimorph piezo-actuator

Figure 12 shows typical FGM structure where the mechanical and physical properties vary along the z-direction.

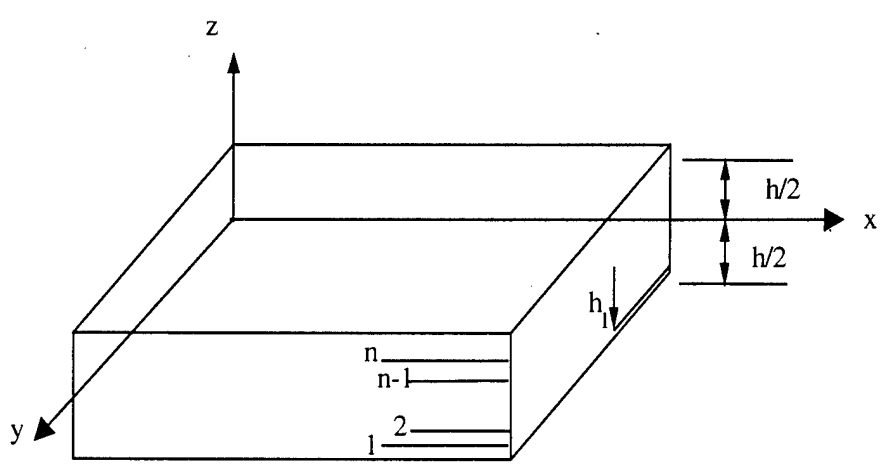

Figure 12 Piezoelectric FGM plate

A piezoelectric laminate consists of n laminae, each being a piezoelectric material with specified electroelastic properties. The constitutive equations of a piezoelectric material in the absence of temperature effects are given by

$$\sigma_{ij} = C_{ijkl}\varepsilon_{kl} - e_{mij}E_m \tag{4}$$

where $\sigma_{ij}, \varepsilon_{ij}$ are the stress and strain tensor components respectively, E_m is the electric field vector component, C_{ijkl} is the elastic stiffness tensor, and e_{mij} are the piezoelectric coefficients. The electroelastic constants of each lamina may be computed from some micromechanical model such as the Eshelby type method as outlined by Dunn and Taya (1993a, b). Two analytical modeling has been established to predict the out-of-plane displacement and stress field of laminated piezoelectric plate, Classical Lamination Theory (CLT) and 2D-elasticity solution.

1.1 Classical Lamination Theory (CLT)

Classical lamination theory (CLT), as found in any composite textbook such as Gibson(1994) assumes a state of plane stress along the z-axis where, $\sigma_z = \sigma_{xz} = \sigma_{yz} = 0$. The constitutive equations of a piezoelectric lamina, eq. 4, under applied electric field in the z direction only, and under the assumption of plane stress along the z-axis, reduces to

$$\begin{Bmatrix} \sigma_x \\ \sigma_y \\ \sigma_{xy} \end{Bmatrix} = \begin{bmatrix} \overline{Q}_{11} & \overline{Q}_{12} & 0 \\ \overline{Q}_{21} & \overline{Q}_{22} & 0 \\ 0 & 0 & Q_{66} \end{bmatrix}_i \begin{Bmatrix} \varepsilon_x^o + z\kappa_x \\ \varepsilon_y^o + z\kappa_y \\ \gamma_{xy}^o + z\kappa_{xy} \end{Bmatrix} - \begin{bmatrix} 0 & 0 & \overline{e}_{31} \\ 0 & 0 & \overline{e}_{32} \\ 0 & 0 & 0 \end{bmatrix} \begin{Bmatrix} 0 \\ 0 \\ E_z \end{Bmatrix} \tag{5}$$

where

$$\begin{aligned} \overline{Q}_{ij} &= C_{ij} - \frac{C_{i3}}{C_{33}} C_{j3} \\ \overline{e}_{ij} &= \frac{C_{i3}}{C_{33}} e_{33} - e_{ij} \end{aligned} \tag{6}$$

It is noted here that $\overline{Q}_{ij}$, $\overline{e}_{ij}$ are the reduced stiffness constants and reduced piezoelectric constants that are modified by the assumption of plane stress and where $\varepsilon_x^o, \varepsilon_y^o$, and ε_{xy}^o are the in-plane strain components at mid-plane, z=0 as shown in Fig. 11, κ_x, κ_y, and κ_{xy} are the curvatures of the plate.

The resultant in-plane forces and bending moments are defined by

$$\{N, M\} = \sum_{i=1}^{n} \int_{h_{i-1}}^{h_i} \{\sigma\}(dz, zdz) \tag{7}$$

carrying out the integration through the plate thickness of h, the resultant forces and bending moments can then be written as

$$\begin{bmatrix} N \\ M \end{bmatrix} = \begin{bmatrix} A & B \\ B & D \end{bmatrix} \begin{Bmatrix} \varepsilon^{o} \\ \kappa \end{Bmatrix} - \begin{bmatrix} N^{E} \\ M^{E} \end{bmatrix} \tag{8}$$

where

$$[A, B, D] = \sum_{i=1}^{n} \int_{h_{i-1}}^{h_i} [\overline{Q}]_i (dz, zdz, z^2 dz) \tag{9a}$$

$$[N, M]^{E} = \sum_{i=1}^{n} \int_{h_{i-1}}^{h_i} [\overline{e}]_i \{E\}(dz, zdz) \tag{9b}$$

where h_{i-1} and h_i are the distance from the bottom of the plate to the bottom and top interfaces of the ith lamina respectively, with $i = 1,2, \ldots n$. Hence the thickness of the ith lamina is then h_i-h_{i-1}. Under the applied electric field or temperature change only, i.e. M=N=0 in eq. (8), the in-plane strain and curvature can be solved as

$$\begin{bmatrix} \varepsilon^{o} \\ \kappa \end{bmatrix} = \begin{bmatrix} a & b \\ b & d \end{bmatrix} \begin{bmatrix} N^{E} \\ M^{E} \end{bmatrix} \tag{10}$$

where

$$\begin{bmatrix} a & b \\ b & d \end{bmatrix} = \begin{bmatrix} A & B \\ B & D \end{bmatrix}^{-1}$$

Under a given electric field throughout the laminate, one can then predict the stress and displacement field of each layer as well as the out-of-plane displacement of the composite plate.

Different types of FGM were studied as shown in the Figure 13 where the conventional bimorph type, one-sided FGM, and FGM bimorph are shown.

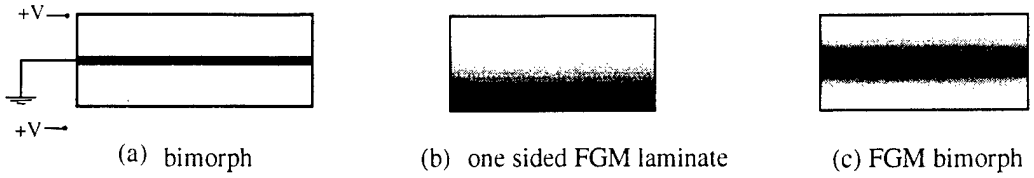

Figure 13 Different types of FGM

The distribution of mechanical and piezoelectric (PZT) properties varies throughout the FGM as shown in Figure 14.

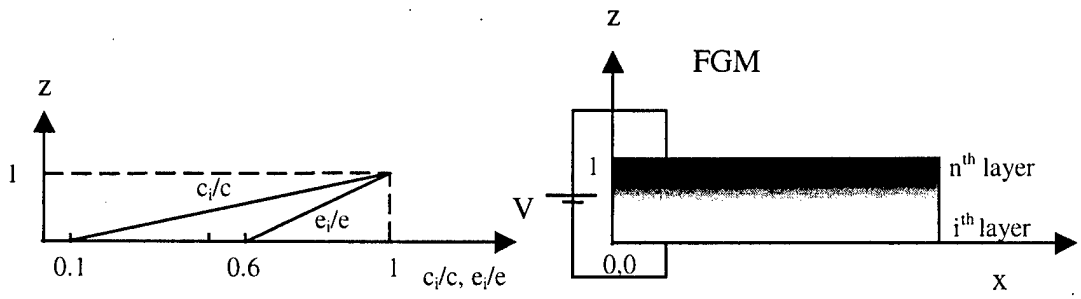

Figure 14 The distribution of mechanical and piezoelectric properties in the FGM

The distribution of both mechanical and piezoelectric properties could be explained through the following formula

$$C_i = [0.1 + 0.225(i-1)]C_{PZT}$$
$$e_i = [0.6 + 0.1(i-1)]e_{PZT} \qquad i = 1,2,.....$$

where C_i, e_i are the mechanical and piezoelectric properties of the i-th layer, respectively. C_{PZT}, e_{PZT} are the mechanical and piezoelectric properties of the piezoelectric material. The mechanical and piezoelectric profile of the FGM bimorph is shown in Figure 15. The properties are increasing toward the middle as FGM-bimorph type A while they are decreasing in FGM-bimorph type B.

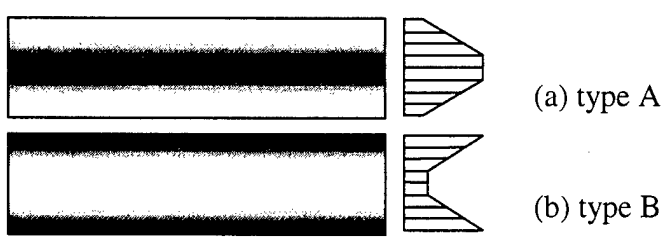

Figure 15 FGM-bimorph profile

The mechanical and piezoelectric properties of the piezoelectric and the mid-plane gold layer are shown in Table 5.

	C_{11} (GPa)	C_{12} (GPa)	C_{13} (GPa)	C_{33} (GPa)	C_{44} (GPa)	e_{31} (C/m^2)	e_{33} (C/m^2)	e_{15} (C/m^2)
PZT	121	75.4	75.2	111	21.1	-5.4	15.8	12.3
Au	101.43	41.63	41.63	101.43	29.9	0	0	0

Table 5 mechanical and piezoelectric properties

The out of plane displacement of each case were calculated and tabulated in Table 6.

Type of FGM microstructure	Standard bimorph, Fig. 2(a)	FGM one-sided, Fig. 2(b)	Bimorph FGM, Fig. 4(a) Type A	Bimorph FGM, Fig. 4(b) Type B
Electric Field (V/mm)	1,000	1,000	1,000	1,000
Applied Voltage (V)	208	500	208	208
Laminate thickness (mm)	0.5	0.5	0.5	0.5
No. of layers	2	5	10	10
Layer thickness(mm)	0.208 Au = 0.082	0.1	0.0416 Au = 0.082	0.0416 Au = 0.082
Curvature (1/m)	0.99	0.992	2.15	0.773
Max. σ_x (MPa)	12.18	8.5	9.8	9.36
Out-of –plane displacement (mm) for plate length of 50mm	0.618	0.62	1.34	0.48

Table 6 Comparison of out-of-plane displacement and maximum in-plane stress for various types of piezo-composite plates

The FGM bimorph with mid-plane layer exhibited the maximum out of plane displacement. The results of the in-plane stresses between layers of each case have been are shown in Figure 16.

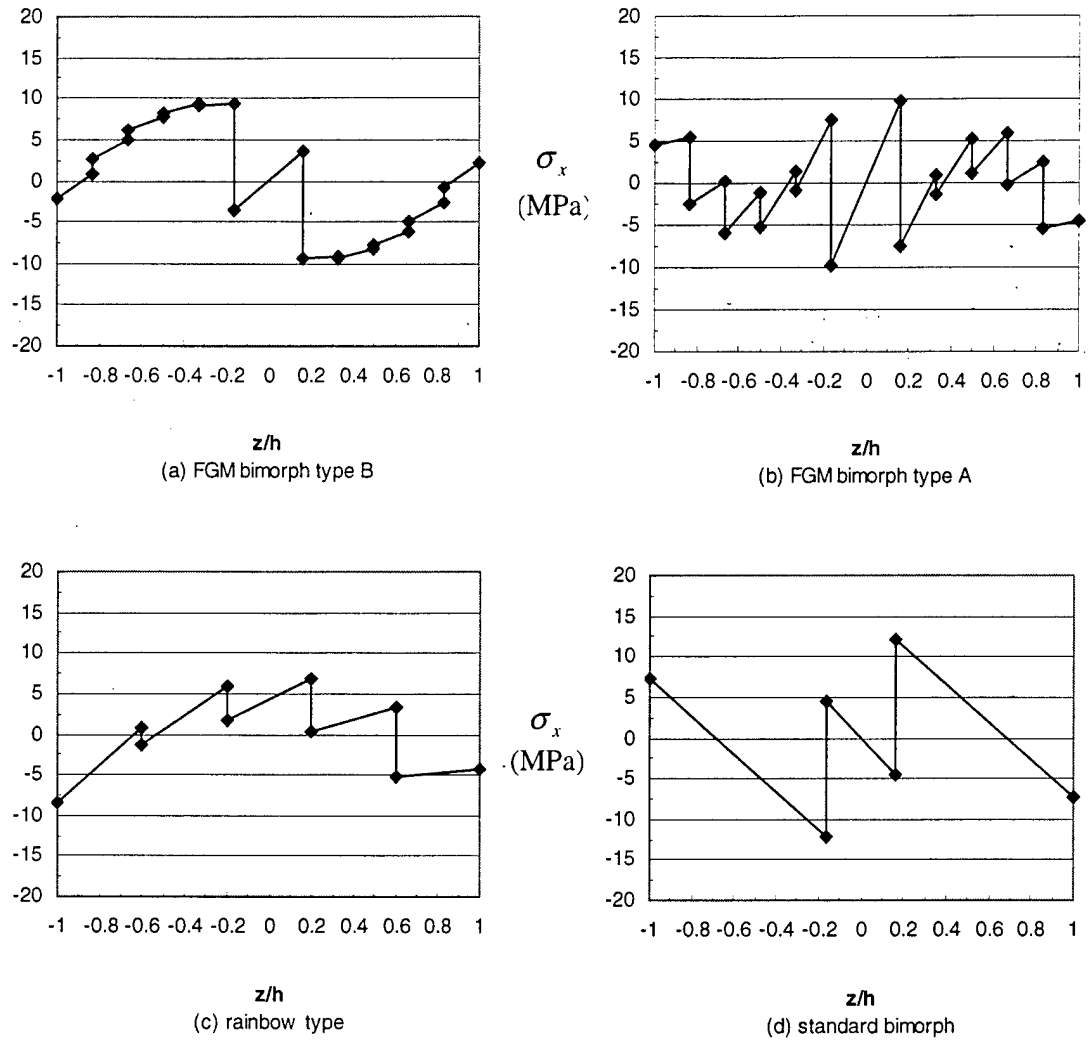

Figure 16 in-plane stresses throughout the plate thickness (z/h)

As it can be seen from the graph, there exist high in-plane stresses between the layers. That stress reached high in the case of bimorph. The high residual stresses have been reduced through the use of FGM especially the FGM bimorph with intermediate layer.

The gold layer serves as relaxation for the piezoelectric since it does not posses piezoelectric properties. There is a need to investigate on the shear stresses associated with the in-plane stresses by using a more accurate model such as FEM.

1.2 2D elasticity model for piezo composite laminates in cylindrical bending

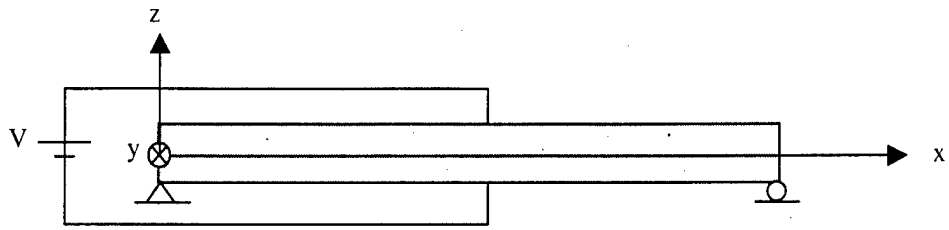

Figure 17 Simply supported piezoelectric plate under a state of plane strain in the y-direction

For a laminate of multi orthotropic layers of piezoelectric material, the cylindrical bending was constructed by following the solution method developed by Pagano (1969) and using the condition of plane strain along the y-direction where, $\varepsilon_y = \varepsilon_{xy} = \varepsilon_{yz} = 0$ as shown in Figure 17. The laminate is simply supported on the ends. The constitutive equations of a piezoelectric material in absence of temperature are given by

$$\varepsilon_{ij} = S_{ijkl}\sigma_{kl} + d_{mij}E_m \tag{11}$$

where $\sigma_{ij}, \varepsilon_{ij}$ are stress and strain tensor components, E_m is electric field vector component, S_{ijkl} are elastic compliance, d_{mij} are the piezoelectric coefficients. The reduced constitutive equations for plane strain is given as,

$$\begin{Bmatrix} \varepsilon_x \\ \varepsilon_z \\ 2\varepsilon_{xz} \end{Bmatrix} = \begin{bmatrix} R_{11} & R_{13} & 0 \\ R_{13} & R_{33} & 0 \\ 0 & 0 & R_{55} \end{bmatrix} \begin{Bmatrix} \sigma_x \\ \sigma_z \\ \sigma_{xz} \end{Bmatrix} + \begin{bmatrix} 0 & 0 & \bar{d}_{31} \\ 0 & 0 & \bar{d}_{33} \\ d_{15} & 0 & 0 \end{bmatrix} \begin{Bmatrix} E_x \\ E_y \\ E_z \end{Bmatrix} \tag{12}$$

where R_{ij} and $\bar{d}_{ij}$ are the reduced compliance and piezoelectric coefficient and are defined as

$$\begin{aligned} R_{ij} &= S_{ij} - \frac{S_{i3}}{S_{33}} S_{j3} \\ \bar{d}_{ij} &= d_{ij} - \frac{S_{i3}}{S_{33}} d_{3j} \end{aligned} \tag{13}$$

where S_{il} and d_{ij} are the compressed forms of S_{ijkl} and d_{mij}.

The boundary conditions of the simply supported piezoelectric laminate are given by

$$\begin{aligned} &\sigma_x(x=0,z) = \sigma_x(x=l,z) = 0 \\ &w(x=0,z) = w(x=l,z) = 0 \end{aligned} \tag{14}$$

while the prescribed surface traction-free conditions of the upper and lower surfaces of the laminate require

$$\sigma_z\left(x,-\frac{h}{2}\right)=\sigma_z\left(x,\frac{h}{2}\right)=0$$
$$\sigma_{xz}\left(x,-\frac{h}{2}\right)=\sigma_{xz}\left(x,\frac{h}{2}\right)=0 \tag{15}$$

The interface continuity conditions at each layer are given by

$$\begin{aligned}
&\sigma_z^i\left(x,\frac{h_i}{2}\right)=\sigma_z^{i+1}\left(x,\frac{h_i}{2}\right)\\
&\sigma_{xz}^i\left(x,\frac{h_i}{2}\right)=\sigma_{xz}^{i+1}\left(x,\frac{h_i}{2}\right)\\
&u_i\left(x,\frac{h_i}{2}\right)=u_{i+1}\left(x,\frac{h_i}{2}\right)\\
&w_i\left(x,\frac{h_i}{2}\right)=w_{i+1}\left(x,\frac{h_i}{2}\right)
\end{aligned}\qquad (i = 1,2, \ldots. N\text{-}1) \tag{16}$$

where i represent the interface ID number between the ith and the $(i+1)^{th}$ laminae with $i = 1 \sim N\text{-}1$ and the topmost and bottommost interfaces are defined as 1st and $(N\text{-}1)^{th}$ interfaces, respectively, while h_i represent the thickness of the ith laminae. The top layer corresponds to $i = 1$ while the bottom layer is $i=N$. The electric field is applied in the z-direction through the thickness of the laminate. The electric field is expressed in the form of Fourier series as

$$E_z = E_o \sum_{n=1,3,5,\ldots}^{\infty} \frac{4}{n\pi}\sin(\lambda x)$$
$$E_x = E_y = 0 \tag{17}$$

where $\lambda = \frac{n\pi}{l}$, and for higher values of n, a nearly constant electric field can be realized.

Following Pagano (1969), the stress field in the ith layer is assumed to be

$$\sigma_x^i = f_i''(z)\sum_n^{\infty}\frac{4}{n\pi}\sin\left(\frac{n\pi}{l}x\right)$$
$$\sigma_z^i = -f_i(z)\sum_n^{\infty}\left(\frac{n\pi}{l}\right)^2\frac{4}{n\pi}\sin\left(\frac{n\pi}{l}x\right) \tag{18}$$
$$\sigma_{xz}^i = -f_i'(z)\sum_n^{\infty}\left(\frac{n\pi}{l}\right)\frac{4}{n\pi}\cos\left(\frac{n\pi}{l}x\right)$$

where $f_i(z)$ is an unknown function to be determined. The equilibrium equations given by

$$\sigma_{ij.j} = 0 \tag{19}$$

are automatically satisfied if eq.(18) is substituted into eq.(19). The 2D-strain compatibility equation is given by

$$2\varepsilon_{xz.xz} - \varepsilon_{z.xx} - \varepsilon_{x.zz} = 0 \tag{20}$$

Substitution of eq.(12) into eq.(20) and use of eqs.(17) and (18) leads to a fourth order ordinary differential equation

$$R_{11}^i f_i''''(z) - \lambda^2 \left(2R_{13}^i + R_{55}^i\right) f_i''(z) + \lambda^4 R_{33}^i f_i(z) = \lambda^2 \bar{d}_{33} E_o \tag{21}$$

The solutions $f_i(z)$ can be expressed by

$$f_i(z) = \sum_{j=1}^{4} A_{ji} \exp\left(m_{ji} z_i\right) + \frac{\left(\bar{d}_{33}\right)^i E_o}{\lambda^2 R_{33}^i} \tag{22}$$

where A_{ji} are constant and the values of m_{ji} are given by

$$\begin{pmatrix} m_{1i} \\ m_{2i} \end{pmatrix} = \pm\lambda \left(\frac{a_i + b_i}{c_i} \right)^{\frac{1}{2}}$$
$$\begin{pmatrix} m_{3i} \\ m_{4i} \end{pmatrix} = \pm\lambda \left(\frac{a_i - b_i}{c_i} \right)^{\frac{1}{2}} \tag{23}$$

where

$$a_i = R_{55}^i + 2R_{13}^i$$
$$b_i = \left[a_i^2 - 4R_{11}^i R_{33}^i\right]^{\frac{1}{2}} \tag{24}$$
$$c_i = 2R_{11}^i$$

The stress field solutions of the ith layer can be found using eq.(22) as

$$\sigma_x^i = \sum_{n=1,3...}^{\infty} \sum_{j=1}^{4} A_{ji} m_{ji}^2 \exp(m_{ji} z_i) \frac{4}{\pi} \sin(\lambda x)$$

$$\sigma_z^i = \sum_{n}^{\infty} \left[\sum_{j=1}^{4} - A_{ji} \exp(m_{ji} z_i) \lambda^2 \frac{4}{\pi} \sin(\lambda x) - \frac{(\bar{d}_{33})^i E_o}{R_{33}^i} \frac{4}{\pi} \sin(\lambda x) \right] \tag{25}$$

$$\sigma_{xz}^i = \sum_{n}^{\infty} \sum_{j=1}^{4} - A_{ji} m_{ji} \exp(m_{ji} z_i) \lambda \frac{4}{\pi} \cos(\lambda x)$$

while the displacement components are found from the strain-displacement relation,

$$u_i = \sum_{n}^{\infty} \left\{ \sum_{j=1}^{4} A_{ji} \exp(m_{ji} z_i) \left[\lambda R_{13}^i - \frac{R_{11}^i}{\lambda} m_{ji}^2 \right] + \left[\frac{R_{13}^i}{R_{33}^i} (\bar{d}_{33})^i - (d_{31})^i \right] \frac{E_o}{\lambda} \right\} \frac{4}{\pi} \cos(\lambda x)$$

$$w_i = \sum_{n}^{\infty} \sum_{j=1}^{4} A_{ji} \exp(m_{ji} z_i) \left[R_{13}^i m_{ji} - \frac{\lambda^2 R_{33}^i}{m_{ji}} \right] \frac{4}{\pi} \sin(\lambda x) \tag{26}$$

It is noted that the above solutions satisfy the boundary conditions of eq.(14) while the surface traction-free boundary conditions of eq.(15) and the interface continuity conditions of eq.(16), remain to be satisfied, resulting *4N* equation for *4N* unknown constants A_{ji}.

Figure 18 shows some of the results obtained by the 2D elasticity model and FEM, the distribution of the inter-laminar shear stress , τ_{xz} and normal stress, σ_x, near the free edge along the longitudinal (x axis) direction.

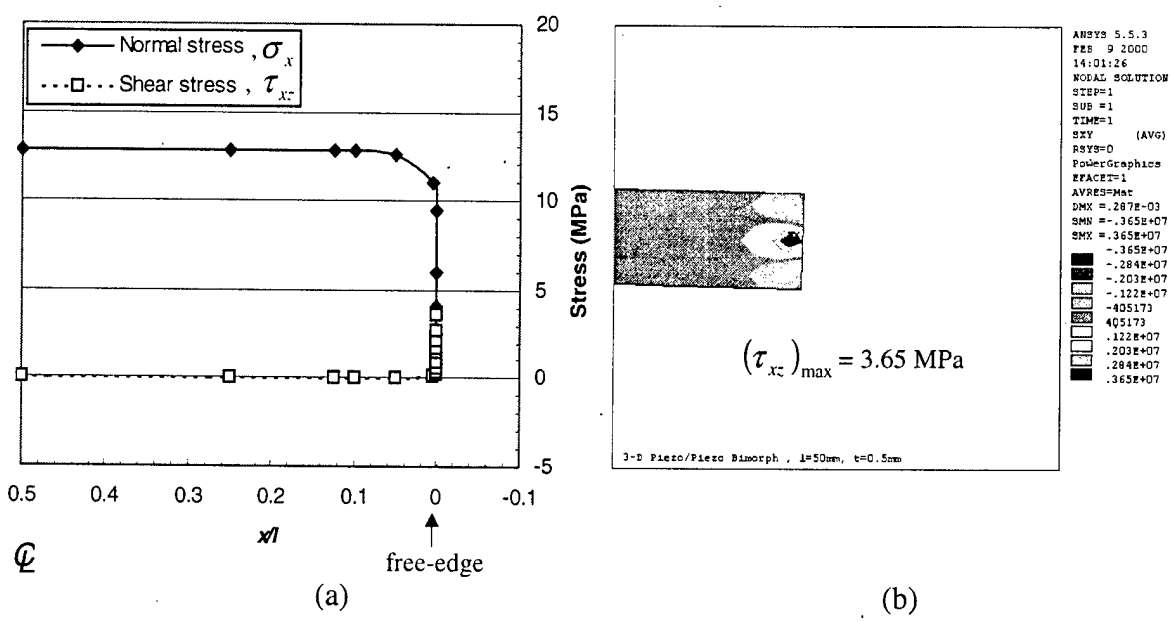

Figure 18 Distribution of normal stress, σ_x and inter-laminar shear stress, τ_{xz} near free edge of a standard bimorph piezo-actuator under applied voltage of 208V, predicted by (a) the 2D elasticity model and (b) FEM

It follows from Fig. 18 that the predicted interlaminar shear stress near the free edge by the 2D elasticity model is close to those by 2D FEM analysis.

2. Material Property Modeling For Fiber Based Piezoelectric FGM Bimorphs

Our work on piezoelectric FGM bimorphs has led to the need for accurate material properties for piezoelectric composites. One possible fabrication method for piezoelectric FGM actuators is through the use of stacked layers of piezo-ceramic fibers. In these devices the fiber volume fraction is graded from layer to layer thereby resulting in graded material properties, including piezoelectric coupling, from layer to layer. Due to the fact that the fiber diameter is nearly the same as the layer thickness within the composite and that within an FGM the fiber distribution is clearly not uniform through the thickness of the composite, a uniform packing of fibers in these devices is not achieved. Because of this deviation from idealized fiber packing many of the assumptions, including matrix connectivity, of most micromechanics models, including those based on Eshelby's (1957) work, are violated. This leads to the use of the finite element method (FEM) for evaluation of individual unit cells. Others have looked at this approach, but they assumed symmetries which are not actually present in reality.

2.1. The Fiber Based Piezoelectric FGM Bimorph

The basic design consists of stacking two piezoelectric FGM's into a symmetric bimorph as shown in Figure 19. The FGM laminates consist of piezoelectric ceramic fibers contained in an epoxy matrix. A second type of fiber, which is not piezoelectric, is used as a "place holder" in the layers with lower piezoelectric fiber volume fraction, v_f, to prevent adjacent layers from being pressed into each other during the cure cycle.

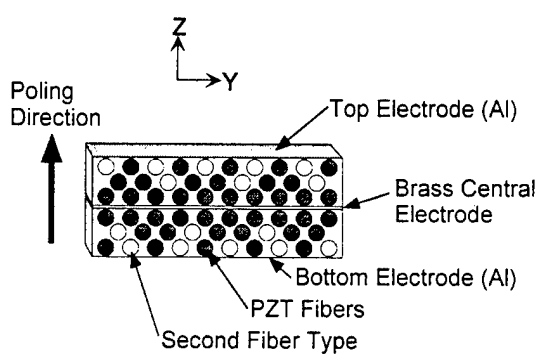

Figure 19. Schematic end view of the fiber based FGM bimorph actuator.

2.2. Modeling Fiber Based Piezoelectric Composite Material Properties

For the case of current piezoelectric fiber composites, the diameter of the fibers is almost as large as the layer thickness and simply examining v_f, does not give an accurate picture of the packing of the fibers. For this reason, the concept of ceramic line fractions in circular fiber composites was used. For this work the line fractions are labeled Y and Z, where Y is the ratio of fiber diameter to fiber centerline spacing within each layer, and Z is the ratio of fiber diameter to layer thickness.

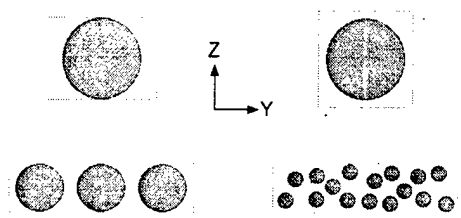

(A) (B)

Figure 20. Rectangular versus square packing of circular fibers in a composite. (A) Rectangular packing, top image showing v_f = .56, Z = .99 and Y = .71. (B) Square packing, top image showing v_f = .56, Z = Y=.84.

This distinction between square and rectangular fiber packing is important as v_f in the FGM layers will be solely a function of Y, the in plane line fraction because all layers are the same thickness. Further, when considering that the dielectric constants of the fiber and the matrix differ by a factor of 100, examination of the top images in Figure 20 indicates that the electric field will be very different in the two different packing arrangements.

To show the deviation from the idealized results of most micromechanics models, it is useful to compare the FEM results to an analytical model. The recently published work of Mikata (2000) allows determination of the Eshelby tensor for a composite where the poling axis is perpendicular to the long axis of the fiber. Even with the limitations discussed above, use of Mikata's Eshelby tensor in the Mori-Tanaka (1973) mean field theory as outlined by Dunn and Taya (1993b) will provide a comparison to the FEM models to be used for material property determination.

The first step in the FEM analysis is to determine which unit cell to use and also which planes of symmetry may be used to minimize the computational effort required to solve the model. For this work the 1/2 symmetric unit cell was chosen as shown in Figure 21.

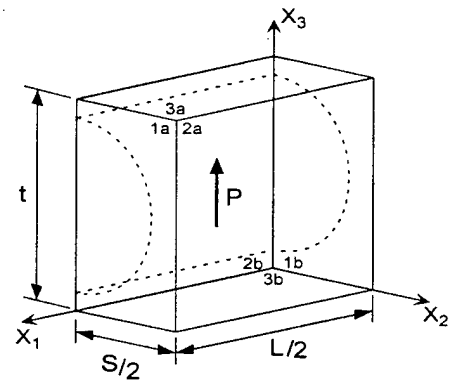

Figure 21. Schematic representation of 1/2 symmetric unit cell with faces labeled for boundary condition application. Poling axis is labeled as P in the figure. Faces 3a and 3b are the surface electrodes.

The choice to use the 1/2 symmetric unit cell which models the entire layer thickness was due to the fact that there is not a plane of electrical symmetry parallel to the 1-2 plane halfway between faces 3a and 3b. This electrical asymmetry is clearly seen from the plot of voltage versus thickness in a layer of the composite as shown in Figure 22.

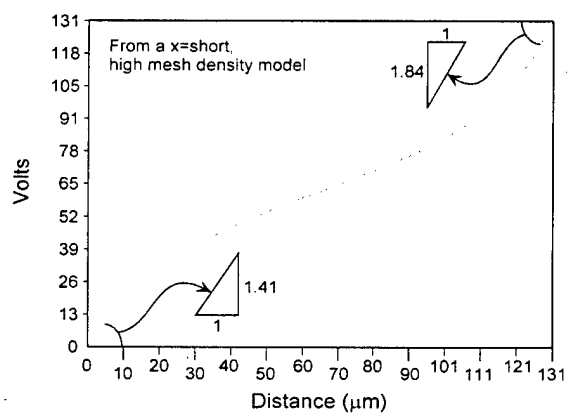

Figure 22. Plot of Voltage versus thickness.

The symmetry planes in this model are faces 1b and 2b or the 1-3 and 2-3 planes. These are clearly planes of mechanical and electrical symmetry. The boundary conditions for this unit cell are listed below in Table 7.

Face	Mechanical B.C.'s	Electrical B.C.'s
1a	All u_1 coupled	$D_1 = 0$
2a	All u_2 coupled	$D_2 = 0$
3a	All u_3 coupled	V coupled
1b	(Symm) $u_1 = 0$	$D_1 = 0$
2b	(Symm) $u_2 = 0$	$D_2 = 0$
3b	All u_3 coupled	V coupled

Table 7. Summary of boundary conditions on FEM 1/2 unit cell.

The model was meshed using 8-node hexahedral elements and a mapped mesh, as shown in Figure 23, as this would provide more accurate results than provided by a free mesh of 4-node tetrahedrons. The choice of the hexahedral elements would also allow easier control of mesh density in areas with high gradients such as the thin layer of matrix material between the fiber and the surface electrodes.

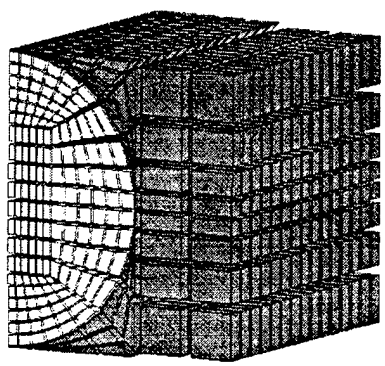

Figure 23. Exploded view of unit cell showing hexahedral elements. Fractions are Z = .99, Y = .56, v_f = .43. Shown in same orientation as unit cell of Figure 4.

The number of elements used in this work ranged from 3540 to 3660. The small range is due to the fact that most of the elements are in the region directly around the fiber and over the small range of Z line fractions considered, the shape of the elements is fairly constant. The solution at this element density was able to quickly converge and there are no poorly shaped elements. The larger number of elements was for the low Y line fraction. The small change added a few more elements in the area between fibers within each layer, although there was not too much concern in this area as the gradients were all fairly low. The practical upper limits of this model are Z = .995 and Y = .97 for v_f = .76, or very close to the maximum v_f of 0.785 for square packed cylindrical fibers.

The effective material properties were then found for a range of Y and Z line fractions by using the FEM method to run a series of hypothetical experiments based on those of Bent and Hagood (1997) with the addition of several new cases to determine the rest of the material properties. These experiments are summarized in Table 8 and the material properties for these calculations are listed in Table 9. It is further noted that in cases 5 through 7, some of the symmetry conditions listed in Table 7 were removed and replaced with a different set of constraints as the symmetric displacements would not always be valid in the shear cases.

Case	Mechanical Loading	Electrical Loading	Properties Obtained
1	$u_i = 0$ on faces 1a, 2a, 3a, 3b (zero strain)	Apply voltage V on top electrode, Ground bottom electrode	e_{31}, e_{32}, e_{33}, ε_{33}
2	Apply displacement u_1 on face 1a u_1 = free on 2a, 3a, 3b $u_2 = u_3 = 0$ on 1a, 2a, 3a, 3b	V = 0 on Electrodes (short circuit)	C_{11}, C_{12}, C_{13}, e_{31}
3	Apply displacement u_2 on face 2a u_2 = free on 1a, 3a, 3b $u_1 = u_3 = 0$ on 1a, 2a, 3a, 3b	V = 0 on Electrodes (short circuit)	C_{12}, C_{22}, C_{23}, e_{32}
4	Apply displacement u_3 on face 3a u_3 = free on 1a, 2a; $u_3 = 0$ on 3b $u_1 = u_2 = 0$ on 1a, 2a, 3a, 3b	V = 0 on Electrodes (short circuit)	C_{32}, C_{32}, C_{33}, e_{33}
5	Apply displacement u_2 on face 3a u_2 = free on 1a, 2a, 2b; $u_2 = 0$ on 3b $u_1 = u_3 = 0$ on 1a, 2a, 2b, 3a	V = 0 on Electrodes (short circuit)	C_{44}, e_{24}
6	Apply displacement u_3 on face 1a u_3 = free on 2a, 3a, 3b; $u_3 = 0$ on 1b $u_1 = u_2 = 0$ on 1a, 1b, 2a, 3a, 3b	V = 0 on Electrodes (short circuit)	C_{55}, e_{15}
7	Apply displacement u_1 on face 2a u_1 = free on 1a, 1b, 3a, 3b; $u_3 = 0$ on 2b $u_2 = u_3 = 0$ on 1a, 1b, 2a, 2b, 3a, 3b	V = 0 on Electrodes (short circuit)	C_{66}

Table 8. Load cases for FEM 1/2 symmetric unit cell.

	C_{11} (Gpa)	C_{12} (Gpa)	C_{13} (Gpa)	C_{33} (Gpa)	C_{44} (Gpa)	e_{31} (C/m^2)	e_{33} (C/m^2)	e_{15} (C/m^2)	$\varepsilon_{11}/\varepsilon_0$	$\varepsilon_{33}/\varepsilon_0$
PZT-5A	121	75.4	75.2	111	21.1	-5.4	15.8	12.3	916	830
Improved Epoxy	10.8	5.7	5.6	10.9	2.7	-0.002	0.007	0.005	7.3	7.3

Table 9. Material properties.

Some of the results of these analyses are plotted below in Figures 24 and 25 along with the results from the micromechanics model using Mikata's Eshelby Tensor as mentioned above. The dashed vertical line is $v_f = 0.785$, or the maximum square packing of round fibers.

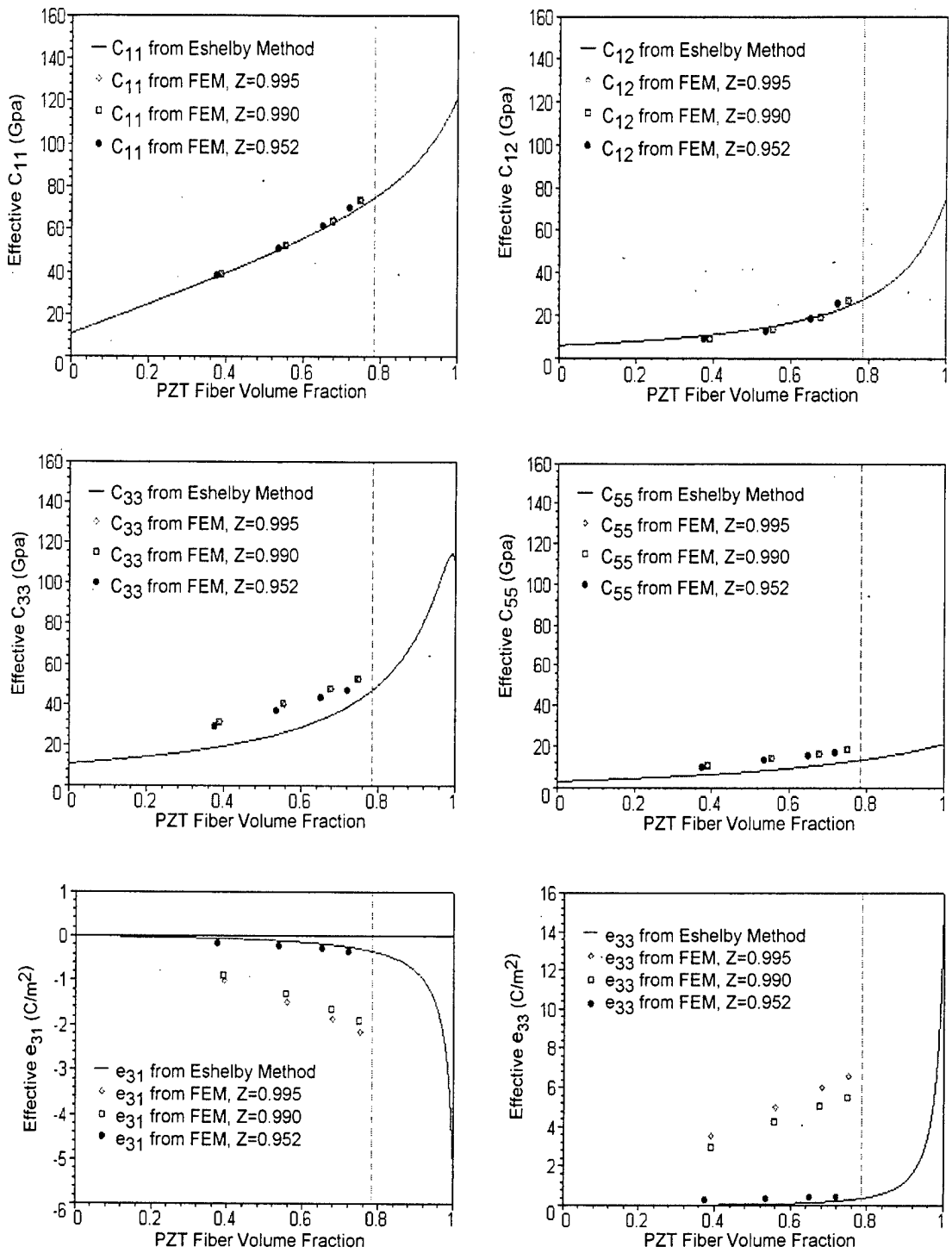

Figure 24. Effective material properties (C_{11}, C_{12}, C_{33}, C_{55}, e_{31}, e_{33}) versus v_f.

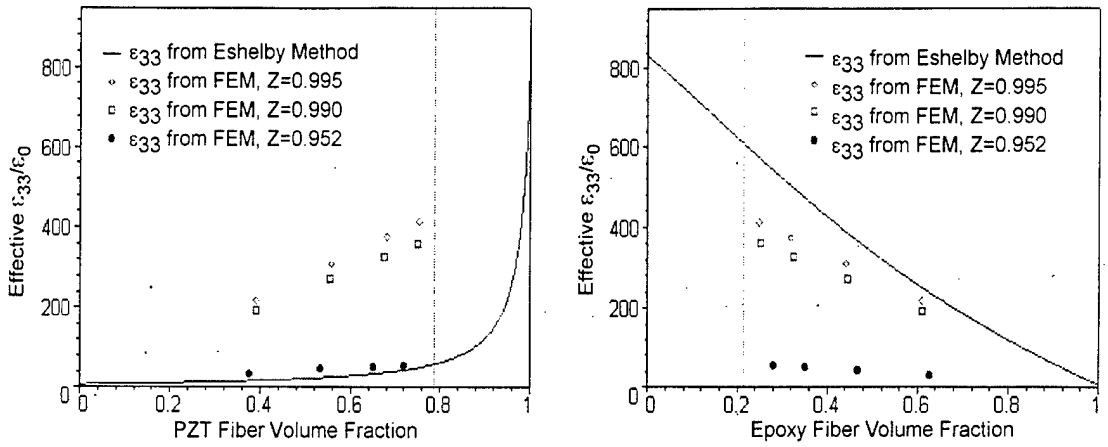

(A) (B)

Figure 25. Effective $\varepsilon_{33}/\varepsilon_0$ versus v_f. (A) Compares FEM results to epoxy (white) matrix Eshelby. (B) Compares FEM results to PZT (black) matrix Eshelby (Note: reversal of volume fractions here.)

From examination of Figures 24 and 25 it is seen that the elastic stiffness constants were independent of different Z line fractions and were predicted reasonably well by the micromechanics model. However, for the piezoelectric and dielectric constants a strong dependence on the Z line fraction was observed, but it was also noted that the results trended towards the micromechanics model as the Z line fraction was reduced. Based on this strong dependence of the piezoelectric and dielectric constants on the Z line fraction, it is important to minimize the thickness of the matrix layer between the fibers and the electrode.

Comparison of Figures 25(A) and 25(B) gives insight into the "black matrix/white matrix" issue over which species is actually the matrix at high v_f. The white matrix case gives the general lower limit for all but the highest Z line fraction and the black matrix case gives an upper limit for Z = 1.

2.3. Analysis Of The Piezoelectric Fiber Based FGM Bimorph

Once the effective composite material properties had been found it was then possible to predict the response of a fiber based FGM bimorph. From the analyzed cases, the middle Z line fraction case of Z = .99 was chosen at a Y line fractions of Y = .93, .71, .50 to represent layers which are all PZT fibers, 2/3 PZT fibers and 1/2 PZT fibers respectively. The actuators as modeled then had three 100 μm thick piezoelectric composite layers on each side of a 25 μm thick brass central electrode with 10 μm thick

aluminum electrodes on the surface for a total thickness of 645 μm and a total length of 50 mm. This represents the type of actuators that are currently being fabricated. These were modeled using ANSYS in the 2D plane stress mode which gives displacements that agree well with a full 3D model, but with much less computational effort. The results for this FGM bimorph are compared to a non-FGM bimorph which was dimensionally identical, but had the effective properties for the Z = .99, Y = .93 layer throughout. Both of these models were subjected to an applied electric field of 500 volts/mm. These results for axial stress, σ_x, are shown below in Figure 26.

From these results it is seen that the FGM bimorph is superior with a tip displacement 187 μm, and a maximum axial stress in the piezoelectric layers of 1.27 MPa compared to 175 μm and 2.08 MPa respectively in the non-FGM bimorph. The reduced stresses are likely due to the gradual build up in stress through the three layers of the FGM instead of the much quicker ramp up evidenced in the single layer of the non-FGM samples. The FGM bimorph also compares very favorably with the results for a monolithic FGM monomorph reported elsewhere, as the tip displacement of our FGM bimorph at 500 volts/mm equates to 37.4 μm/cm bending displacement which is superior to the values of 28 μm/cm for the monolithic FGM monomorph.

Initial comparison of the FGM to non-FGM bimorphs may only show a 7% increase in tip deflection, but there are other benefits to the FGM which go along favorably with this increase. Use of the FGM bimorph as opposed to the non-FGM bimorph has led to a reduction in axial stress of 39%. In addition to this, there is the fact that the FGM only uses about 75% of the expensive ceramic piezoelectric fibers required for a non-FGM bimorph of identical thickness, resulting in significant cost savings and reduced weight.

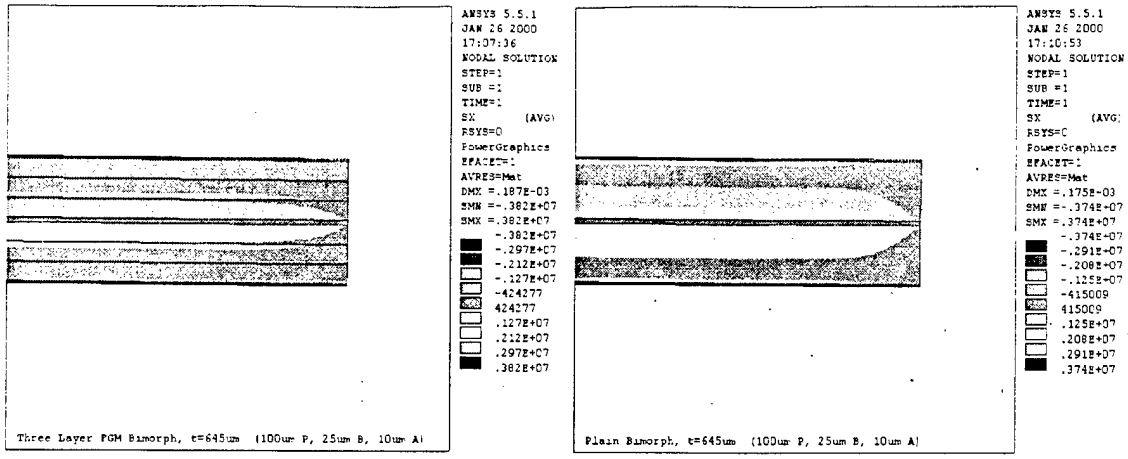

(A) (B)

Figure 26. Results for axial stress, σ_x. (A) FGM bimorph. (B) non-FGM bimorph.

Further examination of the plots in Figure 26 show that the highest stresses are actually in the aluminum surface electrodes. With this in mind, it will be possible to achieve higher displacements by replacing the aluminum foil with a different electrode material that has a lower stiffness (more flexible), such as a conductive polymer film or conductive epoxy paint.

3. Design of Laser Based Displacement Measurement System

To allow accurate measurement of tip displacement induced in the FGM bimorph a laser based displacement measurement system was designed and fabricated as shown below in Figure 27. The use of a laser based transducer allows for non-contact measurement of tip displacement to allow for true no load displacement measurements. The incorporation of and x-y translation stage into the measurement system allows measurements to be easily taken at various points on the specimen. The data acquisition and control of the system is done with a Windows based PC. The accuracy of the system is ±3μm in one location and ±5μm when scanning over a surface using the x-y stage.

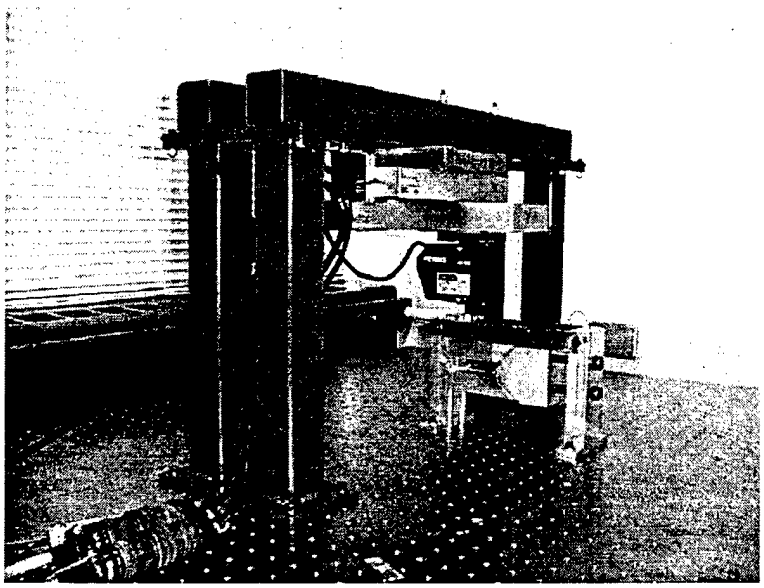

Figure 27. UW Designed and fabricated laser based non-contact displacement measurement system.

4. Concluding Remarks And Future Work

The use of FGM in piezoelectric laminates reduces the stress field while increasing the out-of plane displacement as compared with the standard bimorph. The optimization of the material property gradient profile within the FGM laminae provides higher out-of-plane displacement while reducing the stress field. The CLT and 2D elasticity solution of out-of-plane displacement and stress field are close to those obtained by FEM analysis.

The effective material properties for piezoelectric fiber based composites were predicted by using an FEM model of the fiber unit cell which allowed rectangular fiber packing to be accounted for. It was found that the elastic constants are mostly only a function of the overall volume fraction v_f, while the piezoelectric and dielectric constants were more strongly affected by changing the Z line fraction alone than by changes in v_f.

Using these material properties allowed modeling of piezoelectric fiber based FGM bimorph actuators which are under development and indicates that they have advantages over non-FGM bimorphs and also have higher deflection than for other existing monolithic (non-fiber based) FGM monomorphs.

Fabrication of such actuators is considered to be a key target of our future work, as well as the validation of the analytical modeling as compared to the experimental data. In conclusion, the concept of FGM is found to be very useful in reducing the stress field at the interface where large mismatch in strain exists, thus inducing large stress field, which can be reduced by using the FGM interface design.

5. References

Almajid, A., Taya, M., and Hudnut, S.(2001). Analysis of Out-of-plane displacement and stress field in a piezocomposite plate with functionally graded microstructure, *Intl. J. Solids Structures,* vol. 38, pp.3377-3391.

Bent, A. A., and Hagood, N. W., (1997), "Piezoelectric composites with interdigitated electrodes," *J. Intell. Mat. Sys. and Struct.* **8**, pp. 903-919.

Dunn, M. and Taya, M. (1993a). An analysis of piezoelectric composite materials containing ellipsoidal inhomogeneities, *Proc. Roy. Soc. London* **A443**, 265-287.

Dunn, M. and Taya, M. (1993b). Micromechanics predictions of the effective Electroelastic moduli of piezoelectric composites. *Int. J. solids Structures* **30,**161-175

Eshelby, J. D. (1957). The determination of elastic field of an ellipsoidal inclusion, and related problems, Proc. Royal Soc. London, **A 241**, 376-396

Gibson, R. F. (1994). *Principles of Composite materials and Mechanics,* McGraw Hill

Hudnut, S., Almajid, A., and Taya, M., "Functionally gradient piezoelectric bimorph type actuator", *Proceedings of SPIE meeting on Smart Structures and Materials, March 5-9, 200, New Port Beach, CA, Symposium on Active Materials: Behavior and Mechanics,* SPIE, vol. 3992, pp. 376-386.

Pagano, N. J. (1969). Exact Solution for Composite Laminates Bending, *J. Composite Materials,* **3**, 398-411

Li, Z., Taya, M. and Dunn, M. (1995). Experimental study of fracture toughness of ceramic/ceramic matrix composite sandwich fracture, *J. Am. Ceramic Soc.*, **78**, 1633-39

Mikata, Y., (2000), "Determination of piezoelectric Eshelby tensor in transversly isotropic piezoelectric solids," *Intl. J. Engrg. Science* **38** [6], pp. 605-641.

Mori, T., and Tanaka, K., (1973), "Average stress in matrix and average elastic energy of materials with misfitting inclusions," *Acta Mettal.* **21**, pp. 571-574.

Taya and Arsenault, (1989). Metal Matrix Composites: Thermomechanical Behavior, *Pergamon Press.*

Taya, M., Lee, J. K., and Mori, T. (1997). Dislocation punching from interfaces in functionally graded materials, *Acta materia*, **45**, 2349-2356